



Engineering mode coupling in a hybrid plasmon-photonic cavity for dual-band infrared spectroscopic gas sensing

THANG DUY DAO,^{*}  FLORIAN DUBOIS,  JASMIN SPETTEL, 
ANDREAS TORTSCHANOFF,  CLEMENT FLEURY,  NORBERT
CSELYUSZKA, CRISTINA CONSANI,  ANDRIANOV NIKOLAI, AND
MOHSSEN MORIDI

Sensor Systems, Silicon Austria Labs (SAL), Europastraße 12, 9524 Villach, Austria

**thang.dao@silicon-austria.com*

Abstract: On-chip infrared spectroscopy has become one of the indispensable key technologies for miniature biochemical sensors, gas sensors, food quality control, and environmental monitoring systems. The most important requirement for on-chip spectroscopic sensors is to miniaturize spectroscopic functions to be integrated into thermal emitters and infrared detectors. In this work, we propose a hybrid plasmon-photonic system consisting of a plasmonic grating coupled to a distributed Bragg reflector (DBR)-dielectric-metal cavity for on-chip dual-band spectroscopic sensing applications. The strong coupling between surface-plasmon polaritons and the cavity resonance leads to the hybridization of the photonic states; the mode splitting, the photonic band folding, and the formation of new eigenstates including bound states in the continuum are observed in the system. It is shown that, by engineering the photonic coupling, a dual-band resonant near-perfect absorber is achievable and easily controllable. As a proof of concept, we numerically demonstrate a set of five different dual-band absorbers for CO₂, N₂O, CO, NO, and NO₂ gas sensing applications. The dual-band absorbers can be used for on-chip spectroscopic thermal emitters or infrared detectors in gas sensors. The hybrid plasmon-photonic system can be an attractive photonic platform for applications in emitting and sensing photonic devices.

© 2021 Optical Society of America under the terms of the [OSA Open Access Publishing Agreement](#)

1. Introduction

Miniaturized on-chip spectroscopic devices have attracted considerable industrial interests in the past decades due to their great potential applications in portable chemical sensing and environmental monitoring devices. For example, in the nondispersive infrared (NDIR) sensor such as the carbon dioxide (CO₂) sensor, much effort has been spent on the development of IR spectroscopic filters [1,2], particularly on-chip filtering photonic devices including emitters [3–5] and detectors [6,7]. Among them, the most common spectral filtering structure is the resonant perfect absorber, which can efficiently absorb light in a narrow bandwidth with unity absorptivity [8,9]. Perfect absorber structures typically consist of a confined optical resonator associated with inherent losses of materials, for example antenna-on-insulator-metal layered films [9,10], plasmonic gratings [11,12], Fabry-Perot cavities [13,14] and optical Tamm states [15,16]. Nevertheless, controlling the spectral characteristics in terms of the center wavelength and the spectral bandwidth (full width at half maximum – FWHM) of on-chip spectroscopic devices, which must possess resolutions narrower than the vibration-rotation spectrum of the targeting chemicals, still remains a veritable challenge. Furthermore, most of the gases feature dual-band rotational-vibrational absorption spectra, thus, a dual-band perfect absorber whose resonant branches are identical to the absorption spectra of the sensing gas would be beneficial for NDIR sensors.

Engineering strong coupling in photonic structures has been attracting growing attention over the past decade owing to its broad capabilities in designing exceptional photonic devices which have shown great applications in enhancing light-matter interactions [17,18], quantum information [19,20], low-threshold nano lasers [21,22], and nano-scale sensors [23,24]. The strong coupling in hybrid photonic systems can also be used for engineering photonic bands [25–27], nano lasers [28,29], dual-band absorbers [30,31] and high Q-factor photonic devices associated with quasi-bound states in the continuum (BICs) [32–34]. Azzam et al. have demonstrated a hybrid plasmonic-photonic cavity exploring the formation of BICs due to the symmetry incompatibility with the outgoing fields or destructive interference of the plasmon and photonic resonances [33]. The concept of the hybrid plasmonic-photonic system can be further developed for practical applications.

In this work, we demonstrate a hybrid plasmon-photonic cavity for dual-band spectroscopic sensing applications working in the mid-infrared (MIR) region. The photonic platform utilizes the hybridization between surface-plasmon polaritons (SPPs) and the cavity resonance in a 1D plasmonic grating strongly coupled to an asymmetric distributed Bragg reflector (DBR)-dielectric-metal cavity. It is found that by tuning the geometrical parameters, for example the cavity thickness, the coupling between SPPs and the cavity resonance can be engineered, resulting in different hybridized photonic states including the vacuum Rabi splitting, the photonic band folding and BICs. In particular, a strong dual-band resonance with nearly zero reflectance dips is obtained by tuning the cavity thickness. The wavelengths of both resonant branches and their splitting are also adjustable by changing the structural geometries. As a proof of concept, we demonstrate a set of five different dual-band absorbers for CO₂, N₂O, CO, NO and NO₂ gas sensing in which their dual-resonant branches match perfectly to the dual-band absorption spectra of the sensing gases. This hybrid system can be further extended to visible or longer wavelength regions, providing another photonic platform for engineering resonances in nano-plasmonics for applications in miniaturized spectroscopic emitting and sensing devices.

2. Simulation results and discussion

2.1. Engineering strong coupling in hybrid plasmon-photonic cavity

We first investigate three different photonic systems including a plasmonic grating made of tungsten (Fig. 1(a)), an asymmetric DBR-dielectric-metal cavity (Fig. 1(b)) and a hybrid plasmon-photonic cavity (Fig. 1(c)). The plasmonic grating can be 1D or 2D lattices. Here we choose a 1D grating in which its parameters, including the period – p , the width – w and the height – h , are set to 4.07 μm , 1.3 μm and 0.19 μm , respectively. The asymmetric DBR-dielectric-metal cavity comprises a bottom tungsten film, a dielectric cavity and a top mirror made of three DBR (BaF₂/Si) layers. The chosen number of DBR layers is three which is optimized for the maximum resonant efficiency (zero reflectance or perfect absorptivity). The dielectric cavity can be air or other lossless dielectrics with a thickness – $t_c \sim n \frac{m\lambda}{2}$ (m is an integer, n is the refractive index of the cavity and λ is the resonant wavelength). For example, t_c is set to 1.985 μm for an air cavity. A comparison with a BaF₂ cavity will be discussed in Section 2.3 for gas-sensing application. The hybrid plasmon-photonic cavity is formed by replacing the bottom mirror in the asymmetric cavity by a plasmonic grating. The tungsten layer for all three systems is fixed at 0.2 μm , which is far larger than the penetration depth of the metal in the MIR region to prevent light transmission. The DBR's parameters with $t_{\text{BaF}_2} = 0.660 \mu\text{m}$ and $t_{\text{Si}} = 0.286 \mu\text{m}$ are the same for both asymmetric DBR-dielectric-metal and hybrid plasmon-photonic cavities. We use the rigorous coupled-wave analysis (RCWA, DiffractMOD package from Synopsys' RSoft) for calculating reflectance spectra and band diagrams. The permittivities of tungsten, silicon and BaF₂ are taken from the Brendel-Bormann model by Rakic et al. [35], Palik's handbook [36] and the contractor report by Querry [37], respectively. The refractive index of the air cavity is fixed at 1.

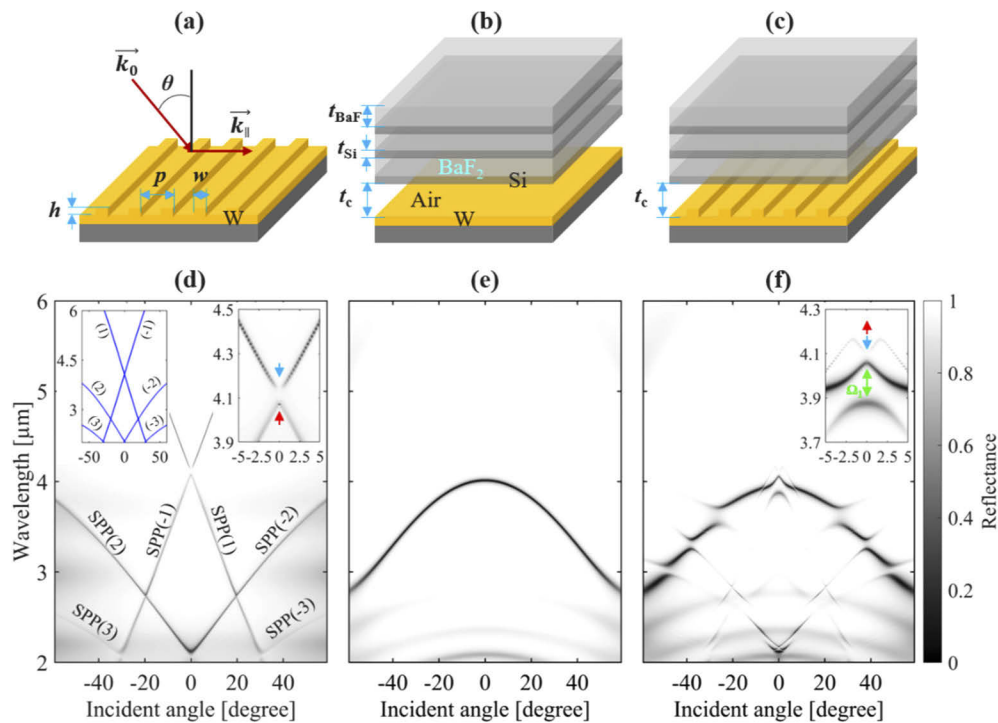


Fig. 1. (a) – (c) Sketches and (d) – (f) simulated angle-dependent reflectance spectra of a plasmonic grating, an asymmetric DBR-dielectric-metal cavity and a hybrid plasmon-photonic cavity, respectively. The metal material for grating, cavity and hybrid plasmon-photonic cavity systems is tungsten, the cavity is air and the DBR comprises three pairs of BaF_2 /Si films. The left inset in (d) represents the calculated SPP's dispersion following Eq. (1) in the plasmonic grating. The right insets in (d) and (f) display zoomed-in spectra between -5° to 5° . For the SPP grating, it is clearly seen that a strong resonance (red arrow) and BIC (blue arrow) appear in the lower-band and upper-band branch of SPP's dispersion, respectively. For the hybrid plasmon-photonic cavity, strong coupling between the cavity resonance and SPPs leads to the formation of vacuum Rabi splitting (denoted by the green arrow with splitting energy $\Omega_1 = 14$ meV), band shifting and band folding in the photonic band. A strong resonance (red arrow) and a BIC (blue arrow) are also observed at normal incidence.

The anomaly absorption of plasmonic gratings was firstly observed by Wood [38], and the theory of plasmon resonance from periodic metallic grating has been developed by Fano [39], Ritchie et al. [40] and Maystre [41]. The origin of photonic gaps and the formation of the discontinued resonance at normal incidence in the SPP's dispersion from a plasmonic grating has been explained in detail by Barnes et al. [11]. The anomaly perfect absorption from plasmonic gratings has been widely used for thermal emitters [42,43] and detectors [44,45]. Figure 1(d) shows the angle-dependent reflectance spectra of the plasmonic grating. For a plasmonic grating, SPPs at the metal-air interface are excited satisfying the matching of SPPs' wavevectors with those of the incident light and the periodic lattice:

$$\vec{k}_{spp} = \vec{k}_{\parallel} + j\vec{G} \quad (1)$$

where $|\vec{k}_{spp}| = k_0 \sqrt{\frac{\epsilon_m}{\epsilon_m + 1}}$, is the wavevector of the SPP at the metal-air interface. Here ϵ_m is the complex permittivity of the metal and $k_0 = \frac{2\pi}{\lambda}$ (λ is the wavelength of the incident light). $|\vec{k}_{\parallel}| = k_0 \sin \theta$ is the projection of the wavevector of light at an incident angle θ . $|\vec{G}| = \frac{2\pi}{p}$, is the primitive lattice vector of the grating with period p ; j is an integer. The dispersion of SPPs following Eq. (1) is shown in the left inset of Fig. 1(d). Interestingly, the numerical simulation result shown in Fig. 1(d) reveals a gap between the two branches of SPPs (see the zoomed-in map in the right inset); at normal incidence, the lower-band branch has a strong and sharp resonance at $4.070 \mu\text{m}$ with a nearly zero reflectance at the crossing between the SPPs^(±1), in contrast, the resonance disappears in the upper-band branch forming a symmetry-protected BIC (denoted by the blue arrow) [33]. For the asymmetric DBR-dielectric-metal cavity, a strong and sharp resonance with an almost zero reflectance is clearly observed in the bandgap of the DBR (Fig. 1(e)). The structure has been proposed by Celanovic et al. [13] and followed by others for thermal emitters [14–16] and detectors [14]. At normal incidence, the cavity has a narrow resonance (FWHM $\sim 3 \text{ nm}$) with an almost zero reflectance at $4.014\text{-}\mu\text{m}$ wavelength nearly following a factor of two compared to the cavity thickness, which is close to the resonance of the plasmonic grating. Figure 1(f) shows the angle-dependent reflectance of the hybrid plasmon-photonic cavity. The hybridization of the plasmonic grating and the asymmetric cavity induces strong coupling between the grating SPPs and the cavity resonance, leading to the mode splitting and hybridized plasmon-polariton photonic states. As seen in the zoomed-in dispersion between $\pm 5^\circ$, and within $3.9 \mu\text{m} - 4.5 \mu\text{m}$ wavelength range, the main cavity resonance is perturbed by the SPPs and split into two bands (denoted by the green arrow). The strong coupling also shifts photonic bands of SPPs to the longer wavelength region. Furthermore, they are folded at near normal incidence, resulting in another resonance (red arrow) in the upper-band branch and a BIC (blue arrow) in the lower-band branch. By tuning the cavity or/and SPPs resonances, the coupling strength and therefore, the hybridized resonances (wavelength, bandwidth, intensity) of the hybrid plasmon-photonic cavity can be engineered depending on the practical applications.

2.2. Engineering dual-band resonance hybrid plasmon-photonic cavity

Figure 2(a) presents the dependence of the reflectance on the cavity thickness in the hybrid plasmon-photonic cavity at normal incidence while the grating parameters and the DBR are kept unchanged. When the cavity thickness approaches $1.985 \mu\text{m}$, a strong coupling between the cavity resonance and the grating's SPPs occurs (denoted by the green arrow) as discussed previously (Fig. 1(f)). Particularly, when the cavity thickness increases close to $2.167 \mu\text{m}$, the second coupling appears, revealing a strong dual-narrowband resonance with almost zero reflectance dips. Figure 2(b) plots the angle-dependent reflectance of the asymmetric DBR-dielectric-metal cavity with a cavity thickness of $2.167 \mu\text{m}$. As the cavity thickness increases, the resonance of the cavity also increases accordingly. At normal incidence, a narrow resonance (28.5-nm FWHM) with a nearly zero reflectance dip is found at $4.302 \mu\text{m}$. The angle-dependent reflectance

of the hybrid plasmon-photonic cavity with the same cavity thickness of $2.167\ \mu\text{m}$ is shown in Fig. 2(c). The hybridization also introduces new hybridized plasmon-polariton photonic bands. Interestingly, around near-normal incidence (inset in Fig. 2(c)), the hybridized states reveal two Friedrich-Wintgen BICs near 1.5 degree incidence and a symmetry-protected BIC at normal incidence (denoted by the blue arrows) [33]. At normal incidence, a strong dual-band resonance (denoted by the red and orange arrows) with nearly zero reflectance dips is observed due to the strong coupling between the cavity resonance and SPPs wherein the upper-band branch is associated with a strong resonance (red arrow).

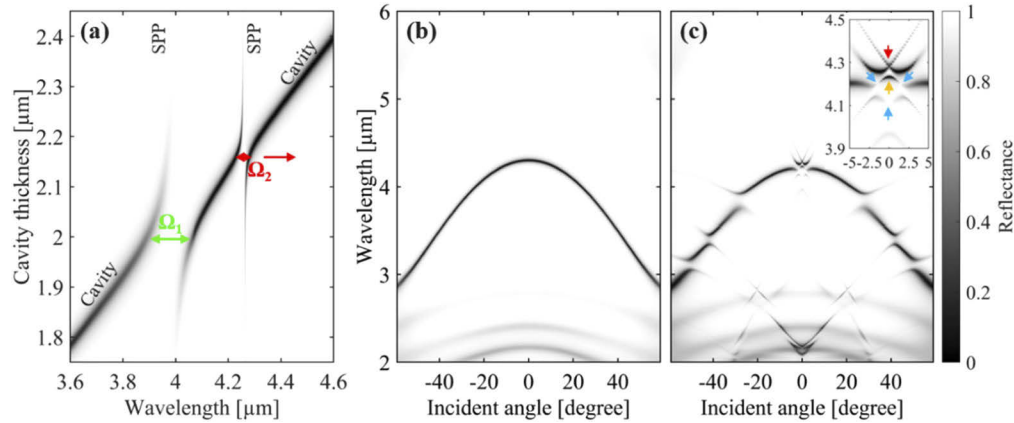


Fig. 2. (a) Simulated reflectance of the hybrid plasmon-photonic cavity with variation of the cavity thickness while keeping the grating parameters unchanged. The second coupling region appears when the cavity thickness varies between $2.1\ \mu\text{m} - 2.2\ \mu\text{m}$ (denoted by red arrow with Rabi splitting energy $\Omega_2 = 3.3\ \text{meV}$); when the cavity thickness approaches $2.167\ \mu\text{m}$, a strong coupling with two intense resonant branches is observed. Simulated angle-dependent reflectance spectra of (b) an asymmetric DBR-metal cavity and (c) a hybrid plasmon-photonic cavity with an equal cavity thickness of $2.167\ \mu\text{m}$ and the same 3-DBR layers ($t_{\text{BaF}} = 0.660\ \mu\text{m}$, $t_{\text{Si}} = 0.286\ \mu\text{m}$). The grating parameters in (a) and (c) are the same with $p = 4.07\ \mu\text{m}$, $w = 1.3\ \mu\text{m}$, $h = 0.19\ \mu\text{m}$. The inset in (c) represents zoomed-in spectra between -5° to 5° . The strong coupling between SPPs and cavity photonic resonances induces new polaritonic bands with a strong dual-band resonance at normal incidence.

Details of resonances at normal incidence of the plasmonic grating, the asymmetric metal-DBR cavity and the hybrid plasmon-photonic cavity with a same cavity thickness of $2.167\ \mu\text{m}$ are represented in Figs. 3(a) – 3(c), respectively. The hybrid plasmon-photonic cavity exhibits a strong dual-band resonance with nearly zero reflectance dips at $4.233\ \mu\text{m}$ (0.007 reflectance) and $4.283\ \mu\text{m}$ (0.042 reflectance) and with narrow bandwidths (14-nm FWHM). We further calculate electric field distributions using the finite-difference time-domain method (FDTD, FullWAVE, Synopsis' RSoft) to elucidate the origin of the resonances (Figs. 3(d) – 3(f)). In the simulation, the electric field propagates along the Z -direction and oscillates along the X -direction (the electric field polarization is perpendicular to the grating grooves). For the plasmonic grating excited at $4.070\text{-}\mu\text{m}$ resonance (Fig. 3(d)), the electric field E_x is confined at the vicinity of the metal strip corners wherein the induced E_z field reveals SPPs at the metal/air interface. In contrast, for the metal-DBR cavity excited at $4.300\text{-}\mu\text{m}$ resonance (Fig. 3(e)), the electric field is strongly confined inside the cavity and there is no induced field in the E_z component. In particular, for the hybrid plasmon-photonic cavity excited at one of the two resonant dips (here at $4.233\ \mu\text{m}$) (Fig. 3(f)), the E_x -component is extremely confined and enhanced not only near the metal strip corners but also inside the cavity while the E_z -component shows strong induced nearfield SPPs at metal/air and also DBR/air interfaces, revealing both cavity resonance's characteristic and the

SPP's origin of the hybrid system. With strong nearfield enhancement in the cavity and induced nearfield at the DBR/air interface, the plasmon-photonic cavity can be a good photonic platform for enhancing light-matter interaction including nearfield-enhanced spectroscopy, vibrational and chemical sensing applications. In the multi-spectral vibrational spectroscopy, it is desirable to have resonances at exact vibrations of the molecules to enhance absorption. The hybridized resonances can be further tuned by changing the grating's parameters. Figure 4(a) manifests the resonance tunability and the detuning of the coupling between the SPP and the cavity resonance by changing the grating period. When the grating period approaches $4.07\ \mu\text{m}$, the strong coupling between the grating SPP and the cavity resonance arises, resulting in a mode splitting with two resonance branches at $4.233\ \mu\text{m}$ and $4.383\ \mu\text{m}$. Furthermore, the coupling strength can also be tuned by adjusting the grating height wherein the resonance shape and width retain almost unchanged.

2.3. Dual-band perfect absorbers for vibrational spectroscopy application

Recent developments of infrared plasmonic and photonic devices have shown a great advancement for enhancing vibrational spectroscopy including surface-enhanced infrared absorption spectroscopy and miniaturized gas sensors. For example, in the gas sensing application, the emission spectra of a thermal emitter can be engineered by using a wavelength-selective absorber in which its emissivity is optimized at nearly unity and with a narrow bandwidth that can efficiently emit infrared light perfectly matching to the absorption band of the sensing gas. On the other hand, an infrared sensor can be also integrated with a narrow band plasmonic absorber, which can sensitively detect light at the absorption band of the sensing gas. In the NDIR sensing, a thermal emitter filtered at the rotational-vibrational spectrum of the targeted gas is often used as the excitation source. Nevertheless, most of diatomic gases feature dual-branch rotation-vibration spectra corresponding to the rotational-vibrational transitions from one rotational level in the ground vibrational state to one rotational level in the excited vibrational state. Two branches of lines are corresponded to the two transition groups with rotation quantum numbers $\Delta J = +1$ and $\Delta J = -1$, which are so-called R-branch (short wavelength) and P-branch (long wavelength), respectively [46]. Thus, a thermal emitter (or a sensor) that has a dual-band resonance matching to the two branches of the targeted diatomic gas is desirable for the NDIR gas sensing application. Here we show that the hybrid plasmon-photonic cavity proposed in this work can be a good photonic platform for on-chip filtering spectroscopic sensors and emitters for gas sensing applications.

Here we demonstrate five different dual-band absorbers targeting at carbon dioxide (CO_2), nitrous oxide (N_2O), carbon monoxide (CO), nitric oxide (NO) and nitrogen dioxide (NO_2) based on the proposed hybrid plasmon-photonic cavity structure. The dual-band absorbers can be used for thermal emitters following Kirchhoff's law wherein the emissivity of an absorber is equal to its absorptivity at thermal equilibrium. They can also be used as the selective absorbing layer for thermal sensors that absorbs radiation at the dual-band resonance and converts absorbed energy into heat. It is worthy to note that in this device platform, since the metal layer of the grating is rather thick ($0.2\ \mu\text{m}$) and does not transmit light in the infrared region, most of the light confined in the cavity is absorbed by this metal grating and the absorptivity is therefore calculated by $1 - \text{reflectivity}$. Figures 5(a) – 5(e) represent the normalized absorption coefficient spectra taken from the HITRAN database [47] (top panels) and the relative absorptivity spectra of the designated dual-band absorbers (middle panels) designed for CO_2 , N_2O , CO , NO and NO_2 , respectively. For the CO_2 -sensing absorber, we use the same structure as shown in Fig. 2(c) and Fig. 3(c) that exhibits a dual-band resonance with two branches located at $4.233\ \mu\text{m}$ (R-branch) and $4.283\ \mu\text{m}$ (P-branch) with nearly perfect absorptivity (0.993 at R-branch and 0.958 at P-branch) (Fig. 5(a)). Following the same procedure made for the CO_2 -gas absorber, the parameters of other gases' absorbers are also obtained. Details of geometrical parameters of all gas-sensing absorbers and their resonances are given in Table 1. All the dual-band resonances of the designated gas sensing

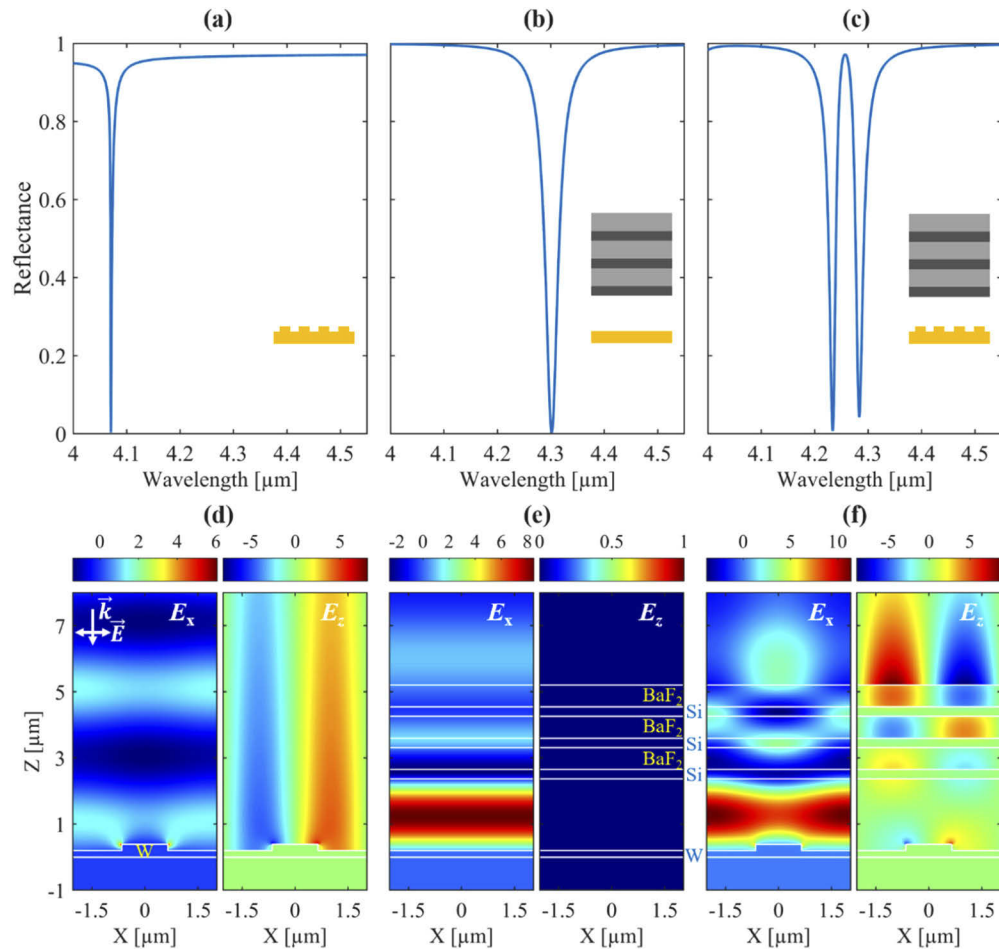


Fig. 3. (a) – (c) Simulated reflectance spectra at normal incidence and (d) – (f) simulated electric fields (E_x and E_z) distribution of a plasmonic tungsten grating, an asymmetric DBR-metal cavity and a hybrid plasmon-photonic cavity, respectively. The resonances of the grating and the cavity are 4.070 μm and 4.301 μm, respectively. The hybrid system reveals a dual-band resonance with two nearly zero dips at 4.233 μm and 4.283 μm (nearly perfect absorption). The grating parameters are the same for (a) and (c), period of 4.070 μm, width of 1.300 μm and height of 0.190 μm. The cavity thickness in (b) and (c) is the same at 2.167 μm. For all full-wave simulations of the electric field distribution, the electric field propagates along the Z-direction and oscillates along the X-direction, and the excited wavelengths are at resonances: 4.070 μm for the grating in (d), 4.301 μm for the cavity in (e) and 4.233 μm for the hybrid plasmon-photonic cavity in (f). The electric fields (E_x and E_z) of the plasmon-photonic cavity manifest a hybridized resonance where the electric field is highly confined in the cavity and the induced field component E_z reveals SPPs.

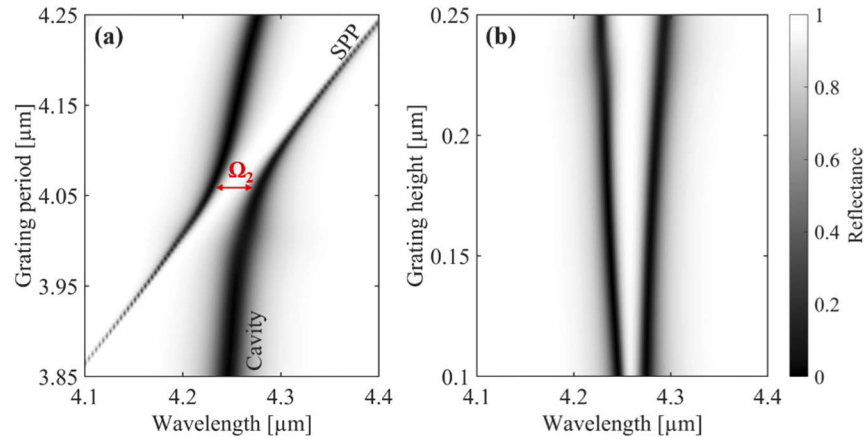


Fig. 4. Simulated dependences of the reflectance on the (a) grating period (with $w = 1.3 \mu\text{m}$, $h = 0.19 \mu\text{m}$) and (b) height (with $p = 4.07 \mu\text{m}$, $w = 1.3 \mu\text{m}$) from a hybrid plasmon-photonic cavity ($p = 4.07 \mu\text{m}$, $w = 1.3 \mu\text{m}$, $h = 0.19 \mu\text{m}$, $t_c = 2.166 \mu\text{m}$). The cavity parameters are the same for (a) and (b) with $t_c = 2.166 \mu\text{m}$, $t_{\text{BaF}} = 0.660 \mu\text{m}$ and $t_{\text{Si}} = 0.286 \mu\text{m}$. The splitting energy (coupling strength) of the dual-band resonance can be tuned by changing the grating height.

absorbers are matching perfectly to the R-branch and P-branch of the absorption spectra of the sensing gases. The bandwidth of each branch in the resonance can be further improved to have a broader resonance maximizing the efficiency of the NDIR sensor by using a smaller number of DBR's period. In this work, we simply keep the same configuration for all the absorbers with the air cavity and three DBR periods, which can provide good thermal insulation for the design of infrared emitters or thermal sensors, particularly when combining with micro-electro-mechanical systems (MEMS) technology. The proposed hybrid plasmon-photonic cavity can also work with other dielectric cavity materials for example BaF_2 , which is also used for the low-refractive index layer of the DBR (BaF_2/Si) in this work. The bottom panels in Figs. 5(a) – 5(e) present simulated spectra of the gas-sensing absorbers using BaF_2 as the cavity with the same 3-DBR (BaF_2/Si) layers. Like air-cavity plasmon-photonic absorbers, the designated BaF_2 -cavity plasmon-photonic systems also exhibit dual-band resonances at the absorption bands of the sensing CO_2 , N_2O , CO , NO and NO_2 gases. Detailed parameters of BaF_2 -cavity gas-sensing absorbers and their resonances are shown in Table 2. As the refractive index of the cavity increases from 1 (air) to 1.467 (BaF_2), the parameters of plasmonic tungsten gratings are also optimized accordingly to obtain the strong coupling between SPPs and cavity resonances.

Table 1. Geometrical parameters of the gas-sensing absorbers with air-cavity

Gas-sensing absorbers	Dual-band resonance [μm]		Grating parameters [μm]			DBR parameters [μm]		Air cavity thickness t_c [μm]
	R-branch	P-branch	p	w	h	t_{BaF}	t_{Si}	
CO_2	4.233	4.283	4.070	1.300	0.190	0.660	0.286	2.167
N_2O	4.470	4.526	4.300	1.370	0.215	0.697	0.302	2.290
CO	4.599	4.737	4.540	1.800	0.320	0.690	0.299	2.341
NO	5.255	5.405	5.160	2.000	0.370	0.807	0.350	2.661
NO_2	6.139	6.239	5.923	1.950	0.400	0.960	0.416	3.154

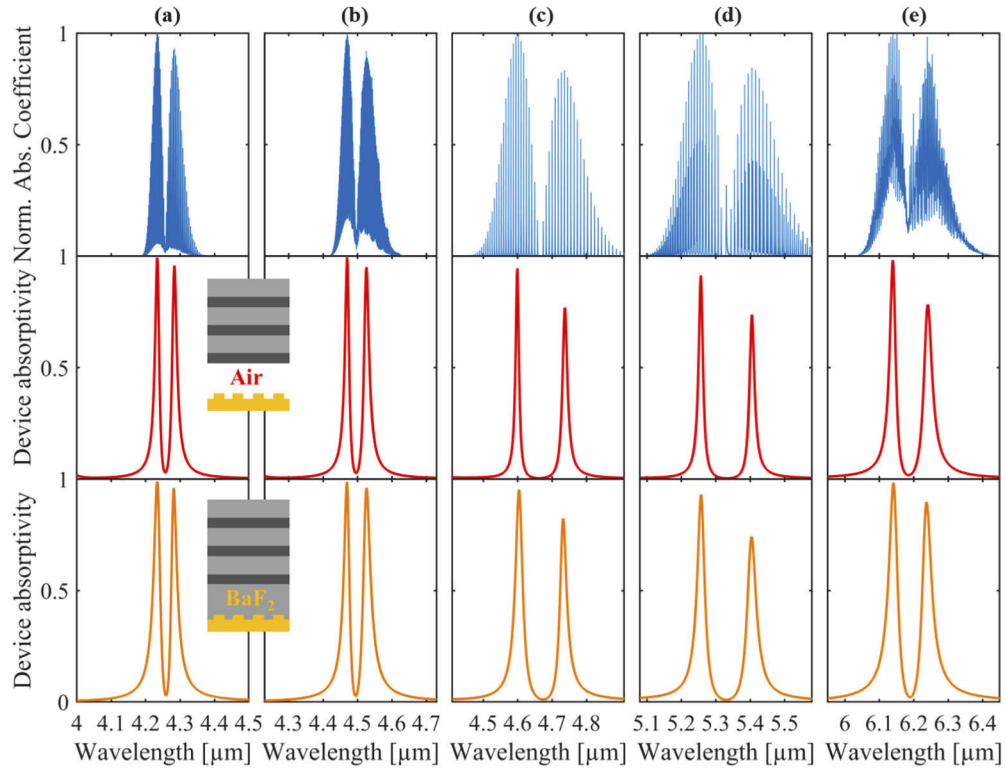


Fig. 5. Application of the hybrid plasmon-photonic cavity for dual-band resonant gas sensing. (a) – (e) Represented absorption coefficient spectra (top) and simulated relative dual-band absorptivity spectra of hybrid plasmon-photonic cavity devices with air cavity (middle panels) and BaF₂ cavity (bottom panels) for CO₂, N₂O, CO, NO, and NO₂ gases, respectively.

Table 2. Geometrical parameters of the gas-sensing absorbers with BaF₂-cavity

Gas-sensing absorbers	Dual-band resonance [μm]		Grating parameters [μm]			DBR parameters [μm]		BaF ₂ cavity thickness t_c [μm]
	R-branch	P-branch	p	w	h	t_{BaF}	t_{Si}	
CO ₂	4.234	4.282	2.558	1.040	1.490	0.660	0.286	1.472
N ₂ O	4.469	4.527	2.700	1.138	0.160	0.697	0.302	1.580
CO	4.603	4.733	2.820	1.430	0.240	0.690	0.299	1.630
NO	5.257	5.404	3.222	1.589	0.285	0.807	0.350	1.862
NO ₂	6.141	6.238	3.745	1.580	0.290	0.960	0.416	2.199

3. Conclusion

In conclusion, we have successfully introduced a simple hybrid plasmon-photonic system consisting of a plasmonic grating coupled to an asymmetric cavity for dual-band absorber spectroscopic sensing applications. We have numerically demonstrated the strategy for engineering the strong coupling between the grating SPPs and the cavity resonance in the hybrid system. The resonant mode splitting, the photonic band folding and the formation of new eigenstates including BICs have been observed in the system. In particular, a dual-band resonant near-perfect absorber is readily accessible, and the resonance is easily tuned in the system by changing the device parameters. Furthermore, we have successfully demonstrated a set of five different absorbers

for CO₂, N₂O, CO, NO and NO₂ gas-sensing applications. The gas-sensing absorbers can be applied for unidirectional thermal emitters and detectors. Although the hybrid plasmon-photonic cavity presented in this work is designed for the MIR region, the system can easily be extended to VIS or far-IR regions, providing another photonic platform for broad applications in lasers, detectors, nonlinear optics, bio-chemical sensing and molecular spectroscopy.

Acknowledgements. This work has been supported by the Federal Republic of Austria, the Styrian Business Promotion Agency (SFG), the Federal State of Carinthia, Upper Austrian Research (UAR) and the Austrian Association for the Electric and Electronics Industry (FEEI) within the “Silicon Austria” PPP research and investment initiative.

Disclosures. The authors declare that there is no conflict of interest.

Data availability. Data underlying the results presented in this paper are not publicly available at this time but may be obtained from the authors upon reasonable request.

References

1. D. Pergande, T. M. Geppert, R. B. Wehrspohn, S. Moretton, and A. Lambrecht, “Miniature infrared gas sensors using photonic crystals,” *J. Appl. Phys.* **109**(8), 083117 (2011).
2. K. Zhou, Q. Cheng, L. Lu, B. Li, J. Song, M. Si, and Z. Luo, “Multichannel tunable narrowband mid-infrared optical filter based on phase-change material Ge₂Sb₂Te₅ defect layers,” *Appl. Opt.* **59**(3), 595 (2020).
3. H. T. Miyazaki, T. Kasaya, M. Iwanaga, B. Choi, Y. Sugimoto, and K. Sakoda, “Dual-band infrared metasurface thermal emitter for CO₂ sensing,” *Appl. Phys. Lett.* **105**(12), 121107 (2014).
4. A. Lochbaum, Y. Fedoryshyn, A. Dorodnyy, U. Koch, C. Hafner, and J. Leuthold, “On-Chip Narrowband Thermal Emitter for Mid-IR Optical Gas Sensing,” *ACS Photonics* **4**(6), 1371–1380 (2017).
5. S. Kang, Z. Qian, V. Rajaram, S. D. Calisgan, A. Alù, and M. Rinaldi, “Ultra-Narrowband Metamaterial Absorbers for High Spectral Resolution Infrared Spectroscopy,” *Adv. Opt. Mater.* **7**(2), 1801236 (2019).
6. A. Lochbaum, A. Dorodnyy, U. Koch, S. M. Koepfli, S. Volk, Y. Fedoryshyn, V. Wood, and J. Leuthold, “Compact Mid-Infrared Gas Sensing Enabled by an All-Metamaterial Design,” *Nano Lett.* **20**(6), 4169–4176 (2020).
7. X. Tan, H. Zhang, J. Li, H. Wan, Q. Guo, H. Zhu, H. Liu, and F. Yi, “Non-dispersive infrared multi-gas sensing via nanoantenna integrated narrowband detectors,” *Nat. Commun.* **11**(1), 5245 (2020).
8. N. Landy, S. Sajuyigbe, J. Mock, D. Smith, and W. Padilla, “Perfect Metamaterial Absorber,” *Phys. Rev. Lett.* **100**(20), 207402 (2008).
9. X. Liu, T. Tyler, T. Starr, A. F. Starr, N. M. Jokerst, and W. J. Padilla, “Taming the Blackbody with Infrared Metamaterials as Selective Thermal Emitters,” *Phys. Rev. Lett.* **107**(4), 045901 (2011).
10. T. D. Dao, K. Chen, S. Ishii, A. Ohi, T. Nabatame, M. Kitajima, and T. Nagao, “Infrared Perfect Absorbers Fabricated by Colloidal Mask Etching of Al–Al₂O₃–Al Trilayers,” *ACS Photonics* **2**(7), 964–970 (2015).
11. W. L. Barnes, T. W. Preist, S. C. Kitson, and J. R. Sambles, “Physical origin of photonic energy gaps in the propagation of surface plasmons on gratings,” *Phys. Rev. B* **54**(9), 6227–6244 (1996).
12. J. Le Perche, P. Quémerais, A. Barbara, and T. López-Ríos, “Why Metallic Surfaces with Grooves a Few Nanometers Deep and Wide May Strongly Absorb Visible Light,” *Phys. Rev. Lett.* **100**(6), 066408 (2008).
13. I. Celanovic, D. Perreault, and J. Kassakian, “Resonant-cavity enhanced thermal emission,” *Phys. Rev. B* **72**(7), 075127 (2005).
14. A. T. Doan, T. D. Dao, S. Ishii, and T. Nagao, “Gires-Tournois resonators as ultra-narrowband perfect absorbers for infrared spectroscopic devices,” *Opt. Express* **27**(12), A725–A737 (2019).
15. Z.-Y. Yang, S. Ishii, T. Yokoyama, T. D. Dao, M.-G. Sun, P. S. Pankin, I. V. Timofeev, T. Nagao, and K.-P. Chen, “Narrowband Wavelength Selective Thermal Emitters by Confined Tamm Plasmon Polaritons,” *ACS Photonics* **4**(9), 2212–2219 (2017).
16. Z. Wang, J. K. Clark, Y.-L. Ho, B. Vilquin, H. Daiguji, and J.-J. Delaunay, “Narrowband Thermal Emission Realized through the Coupling of Cavity and Tamm Plasmon Resonances,” *ACS Photonics* **5**(6), 2446–2452 (2018).
17. J. P. Reithmaier, G. Se, S. Reitzenstein, L. V. Keldysh, V. D. Kulakovskii, T. L. Reinecke, and A. Forchel, “Strong coupling in a single quantum dot–semiconductor microcavity system,” *Nature* **432**(7014), 197–200 (2004).
18. R. Chikkaraddy, B. de Nijs, F. Benz, S. J. Barrow, O. A. Scherman, E. Rosta, A. Demetriadou, P. Fox, O. Hess, and J. J. Baumberg, “Single-molecule strong coupling at room temperature in plasmonic nanocavities,” *Nature* **535**(7610), 127–130 (2016).
19. A. Imamoglu, D. D. Awschalom, G. Burkard, D. P. DiVincenzo, D. Loss, M. Sherwin, and A. Small, “Quantum Information Processing Using Quantum Dot Spins and Cavity QED,” *Phys. Rev. Lett.* **83**(20), 4204–4207 (1999).
20. T. E. Northup and R. Blatt, “Quantum information transfer using photons,” *Nat. Photonics* **8**(5), 356–363 (2014).
21. A. Kodigala, T. Lepetit, Q. Gu, B. Bahari, Y. Fainman, and B. Kanté, “Lasing action from photonic bound states in continuum,” *Nature* **541**(7636), 196–199 (2017).
22. C. Huang, C. Zhang, S. Xiao, Y. Wang, Y. Fan, Y. Liu, N. Zhang, G. Qu, H. Ji, J. Han, L. Ge, Y. Kivshar, and Q. Song, “Ultrafast control of vortex microlasers,” *Science* **367**(6481), 1018–1021 (2020).
23. J.-H. Park, A. Ndao, W. Cai, L. Hsu, A. Kodigala, T. Lepetit, Y.-H. Lo, and B. Kanté, “Symmetry-breaking-induced plasmonic exceptional points and nanoscale sensing,” *Nat. Phys.* **16**(4), 462–468 (2020).
24. J. Wiersig, “Review of exceptional point-based sensors,” *Photonics Res.* **8**(9), 1457 (2020).

25. A. Christ, S. G. Tikhodeev, N. A. Gippius, J. Kuhl, and H. Giessen, "Waveguide-Plasmon Polaritons: Strong Coupling of Photonic and Electronic Resonances in a Metallic Photonic Crystal Slab," *Phys. Rev. Lett.* **91**(18), 183901 (2003).
26. R. Ameling and H. Giessen, "Microcavity plasmonics: strong coupling of photonic cavities and plasmons: Microcavity plasmonics," *Laser Photonics Rev.* **7**(2), 141–169 (2013).
27. L. Ferrier, H. S. Nguyen, C. Jamois, L. Berguiga, C. Symonds, J. Bellessa, and T. Benyattou, "Tamm plasmon photonic crystals: From bandgap engineering to defect cavity," *APL Photonics* **4**(10), 106101 (2019).
28. W. Zhou, M. Dridi, J. Y. Suh, C. H. Kim, D. T. Co, M. R. Wasielewski, G. C. Schatz, and T. W. Odom, "Lasing action in strongly coupled plasmonic nanocavity arrays," *Nat. Nanotechnol.* **8**(7), 506–511 (2013).
29. T. Zhang, S. Callard, C. Jamois, C. Chevalier, D. Feng, and A. Belarouci, "Plasmonic-photonic crystal coupled nanolaser," *Nanotechnology* **25**(31), 315201 (2014).
30. J. Hu, W. Liu, W. Xie, W. Zhang, E. Yao, Y. Zhang, and Q. Zhan, "Strong coupling of optical interface modes in a 1D topological photonic crystal heterostructure/Ag hybrid system," *Opt. Lett.* **44**(22), 5642–5645 (2019).
31. K. Zhou, Q. Cheng, L. Lu, B. Li, J. Song, and Z. Luo, "Dual-band tunable narrowband near-infrared light trapping control based on a hybrid grating-based Fabry–Perot structure," *Opt. Express* **28**(2), 1647 (2020).
32. D. C. Marinica, A. G. Borisov, and S. V. Shabanov, "Bound States in the Continuum in Photonics," *Phys. Rev. Lett.* **100**(18), 183902 (2008).
33. S. I. Azzam, V. M. Shalaev, A. Boltasseva, and A. V. Kildishev, "Formation of Bound States in the Continuum in Hybrid Plasmonic-Photonic Systems," *Phys. Rev. Lett.* **121**(25), 253901 (2018).
34. M. Meudt, C. Bogiadzi, K. Wrobel, and P. Görrn, "Hybrid Photonic–Plasmonic Bound States in Continuum for Enhanced Light Manipulation," **7** (2020).
35. A. D. Rakic, A. B. Djurišić, J. M. Elazar, and M. L. Majewski, "Optical properties of metallic films for vertical-cavity optoelectronic devices," *Appl. Opt.* **37**(22), 5271–5283 (1998).
36. E. D. Palik, *Handbook of Optical Constants of Solids* (Academic Press, 1997).
37. M. R. Querry, *Optical Constants of Minerals and Other Materials from the Millimeter to the Ultraviolet* (Aberdeen Proving Ground, Md.: US Army Armament, Munitions & Chemical Command, Chemical Research & Development Center, 1987).
38. R. W. Wood, "On a Remarkable Case of Uneven Distribution of Light in a Diffraction Grating Spectrum," *Proc. Phys. Soc. London* **18**(1), 269–275 (1902).
39. U. Fano, "The Theory of Anomalous Diffraction Gratings and of Quasi-Stationary Waves on Metallic Surfaces (Sommerfeld's Waves)," *J. Opt. Soc. Am.* **31**(3), 213 (1941).
40. R. H. Ritchie, E. T. Arakawa, J. J. Cowan, and R. N. Hamm, "Surface-Plasmon Resonance Effect in Grating Diffraction," *Phys. Rev. Lett.* **21**(22), 1530–1533 (1968).
41. D. Maystre, "Theory of Wood's Anomalies," in *Plasmonics*, S. Enoch and N. Bonod, eds., Springer Series in Optical Sciences (Springer, 2012), 167, pp. 39–83.
42. M. Laroche, C. Arnold, F. Marquier, R. Carminati, J.-J. Greffet, S. Collin, N. Bardou, and J.-L. Pelouard, "Highly directional radiation generated by a tungsten thermal source," *Opt. Lett.* **30**(19), 2623 (2005).
43. J. Liu, U. Guler, A. Lagutchev, A. Kildishev, O. Malis, A. Boltasseva, and V. M. Shalaev, "Quasi-coherent thermal emitter based on refractory plasmonic materials," *Opt. Mater. Express* **5**(12), 2721 (2015).
44. S. Ogawa, K. Okada, N. Fukushima, and M. Kimata, "Wavelength selective uncooled infrared sensor by plasmonics," *Appl. Phys. Lett.* **100**(2), 021111 (2012).
45. T. D. Dao, S. Ishii, A. T. Doan, Y. Wada, A. Ohi, T. Nabatame, and T. Nagao, "An On-Chip Quad-Wavelength Pyroelectric Sensor for Spectroscopic Infrared Sensing," *Adv. Sci.* **6**(20), 1900579 (2019).
46. S. Albert, K. K. Albert, H. Hollenstein, C. M. Tanner, and M. Quack, "Fundamentals of Rotation–Vibration Spectra," in *Handbook of High-resolution Spectroscopy* (American Cancer Society, 2011).
47. I. E. Gordon, L. S. Rothman, C. Hill, R. V. Kochanov, Y. Tan, P. F. Bernath, M. Birk, V. Boudon, A. Campargue, K. V. Chance, B. J. Drouin, J.-M. Flaud, R. R. Gamache, J. T. Hodges, D. Jacquemart, V. I. Perevalov, A. Perrin, K. P. Shine, M.-A. H. Smith, J. Tennyson, G. C. Toon, H. Tran, V. G. Tyuterev, A. Barbe, A. G. Császár, V. M. Devi, T. Furtenbacher, J. J. Harrison, J.-M. Hartmann, A. Jolly, T. J. Johnson, T. Karman, I. Kleiner, A. A. Kyuberis, J. Loos, O. M. Lyulin, S. T. Massie, S. N. Mikhailenko, N. Moazzen-Ahmadi, H. S. P. Müller, O. V. Naumenko, A. V. Nikitin, O. L. Polyansky, M. Rey, M. Rotger, S. W. Sharpe, K. Sung, E. Starikova, S. A. Tashkun, J. V. Auwera, G. Wagner, J. Wilzewski, P. Wcisło, S. Yu, and E. J. Zak, "The HITRAN2017 molecular spectroscopic database," *J. Quant. Spectrosc. Radiat. Transfer* **203**, 3–69 (2017).